

Effect of SDS and PVP surfactants on synthesis of a flower-shaped porous Ni-MOF_{BDC}@C as electrode materials for high performance supercapacitor

Ningkuan Zhong¹, Weiyi Wu¹, Fen Xu,^{1,2*} Lixian Sun^{1,2*}, Yi Wu^{1,3}, Jianhao Lao¹, Xiaohui Qin¹, Yu Wang¹, Xiangpeng Ding¹, Aicheng Peng³, Jincheng Liu³, Dingding Yuan^{3*}

¹ Guangxi Key Laboratory of Information Materials, Guangxi Collaborative Innovation Center of Structure and Property for New Energy and Materials, 541004, P. R. China

² School of Material Science and Engineering, Guilin University of Electronic Technology, Guilin, 541004, P. R. China

³ EVE Power Co.,Ltd, JingMen, 448000, P. R. China

*E-mail: xufen@guet.edu.cn or 1732211579@qq.com, sunlx@guet.edu.cn, yuandingding@evebattery.com

Received: 8 February 2022 / Accepted: 9 March 2022 / Published: 5 April 2022

In this work, a flower-like porous Ni-MOF_{BDC}@C (MOFs@C_{SP}) has been synthesized successfully on carbon material through two surfactants (SDS and PVP) control by means of a facile solvothermal method. SEM results reveal that the MOFs@C_{SP} is the porous material that bends and folds into the flower shape of Ni-MOF nano sheets orientated grown on the carbon materials. The results also illustrate that the carbon material plays the role of template and conductive reinforcing agent. Under the action of carbon and double surfactants, the MOFs@C_{SP} has the highest specific capacity and the lowest resistance of charge transfer in the four Ni-MOF_{BDC} materials (namely MOFs@C_{SP}, MOFs@C_P, MOFs@C_S and Ni-MOF_{BDC}). That is the specific capacity of MOFs@C_{SP} is 1350.1 F g⁻¹ at 1 A g⁻¹, corresponding to resistance of charge transfer of 0.3 Ω. Moreover, the energy density of the asymmetric device assembled by MOFs@C_{SP} is 42.9 Wh kg⁻¹ under 813.1 W kg⁻¹.

Keywords: supercapacitor; carbon material; surfactant; nickel-metal-organic framework

1. INTRODUCTION

With the continuous development of the social economy and technology and the sharp increase in the demand for energy, human beings are facing fossil fuel energy shortages and environmental pollution. To effectively solve these problems and make up for the intermittent supply of new green energy storage problems (such as solar, wind, hydrogen and other new green energy), seeking more powerful energy storage technologies has become a topic of concern [1,2]. Supercapacitors, which are also called electrochemical capacitors (ECs), have enormous economic value and broad application

prospects for energy storage components [3]. Supercapacitors (SCs) have attracted considerable attention due to their high-power density, long cycle life and rapid charge and discharge rates [4-6]. In general, SCs store energy in three main ways: rapid adsorption and desorption of electrolyte ions at the electrode/electrolyte interface, surface-controlled redox reactions occurring on or near the electrode surface, and diffusion-controlled redox reactions occurring throughout the electrode [7-10]. Obviously, the energy storage process of SCs is mainly carried out on electrodes, so the structure and properties of electrode materials play a key role in achieving efficient energy storage [11,12]. The electrode materials widely used in SCs can be classified into several categories, including carbon-based materials [13], metal oxides [14], conducting polymers [15] and metal-organic framework (MOF)-based materials [16,17].

Metal-organic frameworks (MOFs) are reticular crystalline materials formed by the coordination bonds between organic ligands containing oxygen or nitrogen and transition metal ions [18,19]. MOFs have a large specific surface area, adjustable pores and diverse structures. The electrochemical activity of the material can be improved by adjusting the structure and porosity of the metal-organic framework to expose more active sites [20]. Chen [21] obtained a novel Zn-doped Ni-MOF electrode material by a solvothermal method. They found that the Zn-doped Ni-MOF had excellent electrochemical properties. The specific capacity of the Zn-doped Ni-MOF reached 237.4 mA h g⁻¹ at a current density of 1 A g⁻¹. Its specific capacity remained at 122.3 mA h g⁻¹ as the current density was increased to 20 A g⁻¹. Moreover, its capacity was reduced by 12% after 4000 cycles of a constant current charge and discharge test, which indicated that the Zn-doped Ni-MOF electrode material had excellent redox reversibility. It was thought that the honeycomb structure and smaller microsphere morphology of the Zn-doped Ni-MOF were beneficial for increasing the effective contact area with the electrolyte. On this occasion, more active sites were exposed to participate in the electrochemical reaction, resulting in good electrochemical characteristics.

Carbon electrode materials are porous materials with abundant pores, large specific surface areas, good electrical conductivity and stable chemical properties [22]. As a matrix material, carbon electrode material can not only play the role of a frame but also promote the improvement of the overall conductivity and thermal conductivity of the material [23]. Mei [24] designed nickel-cobalt pyrophosphate/nitrogen-doped carbon (NiCoPN/C) with a hierarchical porous structure and a surface area of 341.7 m² g⁻¹. The specific capacitance of the material was 1240 F g⁻¹ at a current density of 1 A g⁻¹. When the specific power of the NiCoPN/C-5//AC asymmetric supercapacitor was 0.32 kW kg⁻¹, the specific energy reached 50.75 Wh kg⁻¹. The specific capacitance retention was 83.7% after 10, 000 cycles. This study provides a new idea for designing transition metal and heteroatom-doped porous carbon materials for mixing supercapacitor electrodes.

In this study, Ni-MOF_{BDC} was grown on carbon materials by using terephthalic acid as the ligand and QK (okra) porous carbon as the matrix, and a flower-like porous morphology was formed under the induction of sodium dodecyl sulfate (SDS) and polyvinylpyrrolidone (PVP). The structure and electrochemical performance of the capacitor device with the Ni-MOF_{BDC}@C composite as the electrode were studied. The research results showed that the specific capacitance of MOFs@C_{SP} reached 1350.1 F g⁻¹ at a current of 1 A g⁻¹; its energy density was 42.9 Wh kg⁻¹ corresponding to a power density of 813.1 W kg⁻¹. After 5000 cycles, the coulombic efficiency only decreased by 5.2%.

The excellent electrochemical properties of Ni-MOF_{BDC}@C display its good application prospects in the energy storage field.

2. EXPERIMENTAL

2.1 Materials preparation

Polyvinylpyrrolidone (PVP), Sodium dodecyl sulfate (SDS, 99%) and Polytetrafluoroethylene (PTFE) were purchased from Shanghai Aladdin biochemical technology co. Ltd. Ethanol (C₂H₅OH), N, N-dimethylformamide (DMF), Nickel (II) acetate tetrahydrate (Ni(CH₃COO)₂·4H₂O) and p-phthalic acid (PTA, 99%) were obtained from Xilong Scientific Co. Ltd. All reagents were used without further treatment or purification. All aqueous solutions were prepared with high-purity de-ionized water (DI-water, resistance 18 M Ω cm⁻¹).

2.2. Preparation of active carbon from okra seed

Firstly, the okra seed was washed by distilled water and dried in an air-blast drying box at 85 °C for 48 h. Then, the dried okra seed was broken into small pieces and calcined in a tube furnace at 450 °C for 1.5 h under a nitrogen atmosphere to obtain carbon precursor. The carbon precursor and potassium hydroxide were mixed at a mass ratio of 1.0: 3.0, and the activation process was conducted in a tube furnace at 750 °C for 2 h under a nitrogen atmosphere. The product was soaked with a 1 M HCl solution and filtered with distilled water until the filtrate was neutral. The precipitate was finally dried and ground to obtain the okra-seed-based multi-hole carbon material, which called as QK.

2.3. Synthesis of Ni-MOF_{BDC}

Typically, 0.1326 g (0.75mmol) of Ni(CH₃COO)₂·4H₂O was added into 15 mL deionized water to obtain solution A, 0.0083 g (0.5 mmol) of p-phthalic acid (PTA) was dissolved in 30 mL DMF/C₂H₅OH (v/v = 1:1) to obtain solution B. Next, the solution A was added to the solution B under stirring to obtain a stable solution. The mixed solution was then transferred into 100 mL autoclave with a Teflon liner, which heated at 160°C for 24 h. The obtained sample was cooled until room temperature and then it was washed with deionized water and ethanol. Finally, the product was dried in the air.

2.4. Synthesis of Ni-MOF_{BDC}@C by surfactant-assisted

The synthesis method was similar to the part of 2.3. The difference is that 5 mg QK was added into the above solution B under stirring to obtain solution C. And SDS (0.25g), PVP (0.25g) or SDS (0.25g)-PVP (0.25g) were added at the mixed solution (solution A and solution C) before it was transferred into an autoclave. The products obtained were successively named as Ni-MOFs@Cs, Ni-MOFs@C_P and Ni-MOFs@C_{SP}.

2.5 Characterizations

The microstructural analysis of sample was tested by powder X-ray diffraction (XRD; D8 Advance Bruker), which was conducted at 40 kV and 40 mA with a Cu K α radiation ($\lambda = 0.15406$ nm). The 2θ range is 5-90° with 0.02° step increments. The morphologies and elemental analysis of sample were characterized by scanning electron microscope (SEM, SU8010, HITACHI) with energy-dispersive X-ray spectroscopy (EDS; S4800, Hitachi) and transmission electron microscopy (TEM; Tecnai G2 F20, FEI Company). A Thermo Fisher Nicolet 6700 spectrometer (FT-IR; 6700, Nicolet) was used to obtain an IR spectroscopy of sample.

2.6 Electrochemical measurements

Electrochemical performances were performed on a CHI 660E instrument in a three-electrode system, including galvanostatic charge-discharge (GCD), cyclic voltammogram (CV) and electrochemical impedance (EIS). Here, a platinum electrode was chosen as the counter electrodes and a Hg–HgO electrode was used as the reference electrodes. 3.0 M KOH aqueous solution was prepared as the electrolyte. A mixture (active materials, acetylene black and polytetrafluoroethylene (PTFE) with the weight ratio of 80:10:10) was coated on a (1cm \times 1cm) nickel foam and was pressed to a thin foil at a pressure of nearly 10.0 MPa.

The results of galvanostatic charge-discharge (CGD) were used to calculate the specific capacity of the electrode material by equation (1) and (2):

$$C_a = \frac{I \times \Delta t}{S \times \Delta V} \quad (1)$$

$$C_s = \frac{I \times \Delta t}{m \times \Delta V} \quad (2)$$

where C_a (F \cdot cm $^{-1}$), C_s (F \cdot g $^{-1}$), I (A), S (cm 2) and m (g $^{-1}$) are the area specific capacity and mass specific capacity, the discharge current, the contact surface area of the working electrodes and mass of the active materials, respectively. And Δt (s), ΔV (V) refer to discharge time and voltage range, respectively.

The asymmetric supercapacitor devices were assembled using Ni-MOF_{BDC}@C as a positive electrode and activated carbon (QK) as a negative electrode. In the asymmetric supercapacitor device, according to the charge balance $q^+ = q^-$, where $q = m \times C \times \Delta V$; and the mass ratio of electrode is required to conform the equation (3):

$$\frac{m^+}{m^-} = \frac{\Delta V^+ \times C^-}{\Delta V^- \times C^+} \quad (3)$$

where m^+ , m^- , ΔV^+ , ΔV^- and C^+ , C^- represent the mass, potential, specific capacities of the positive electrode and negative electrode, respectively.

The energy density (E) and power density (P) are determined by Eq. (4) and (5):

$$E = \frac{C_s \times \Delta V^2}{2 \times 3.6} \quad (4)$$

$$P = \frac{3600E}{\Delta t} \quad (5)$$

where C_s is the total capacitor of the asymmetric; ΔV is the potential window; Δt is the discharge time.

3. RESULTS AND DISCUSSION

3.1. Structure and morphology

The SEM of the as-prepared QK is shown in Fig. 1. Fig. 1 shows that QK is a porous carbon material with a pore distribution ranging from 500 nm to 10 μm . The abundant micropores can provide channels for the storage and transportation of electrolyte ions, thereby improving the conductivity of the material [25].

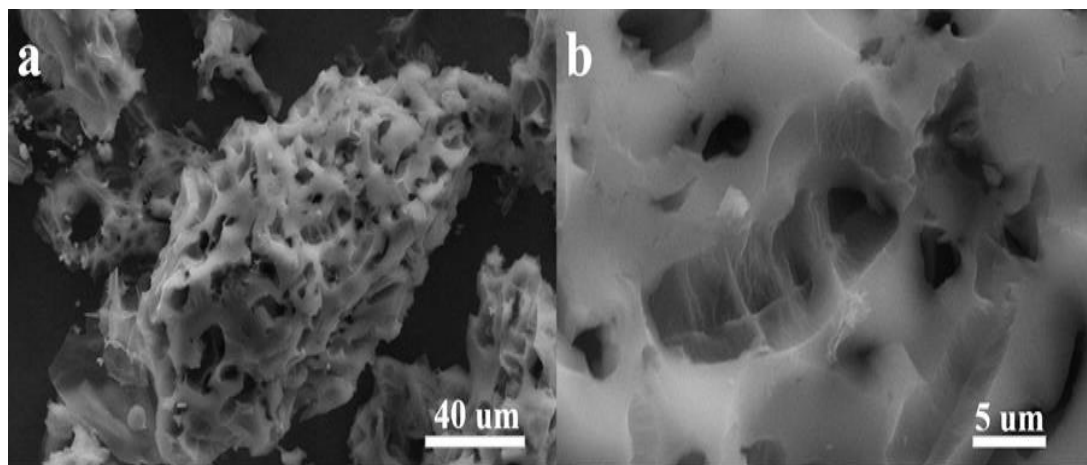


Figure 1. SEM images of QK at different magnification

Fig. 2a, 2b and 2c show SEM images of the MOFs@C_P composite. Compared with Fig. 1, they indicate that Ni-MOF_{BDC} grows on the surface of the carbon material and is densely stacked into a large number of pores with different diameters under the aid of PVP alone. Fig. 2d, 2e and 2f show that part of the Ni-MOF_{BDC} grows on the surface of the carbon material with the aid of SDS only, and another part is not combined with the carbon matrix but grows into a nanoflower structure alone. Fig. 2g, 2h and 2i) show SEM images of MOFs@C_{SP} with the simultaneous assistance of two surfactants (PVP and SDS), which indicate that Ni-MOF_{BDC} consists of nanosheets that grow along the direction of the QK channel. These nanosheets are bent and folded into a flower shape, resulting in the formation of the MOFs@C_{SP} porous structure. Compared with MOFs@C_P (see Fig. 2a, 2b and 2c), the open porous structure of MOFs@C_{SP} can expose more metal active sites, and it can be predicted that it will have better electrochemical performance. Fig. 2i is the SEM image of MOFs@C_{SP} under high magnification; this figure indicates that the thickness of Ni-MOF_{BDC} flakes grown on the surface of carbon QK is 20-50 nm, and the gap between the flakes is 20-100 nm. This kind of layer supports each other and brings many voids, so it can effectively shorten the migration path of ions and enhance the conductivity of MOFs@C_{SP} [26].

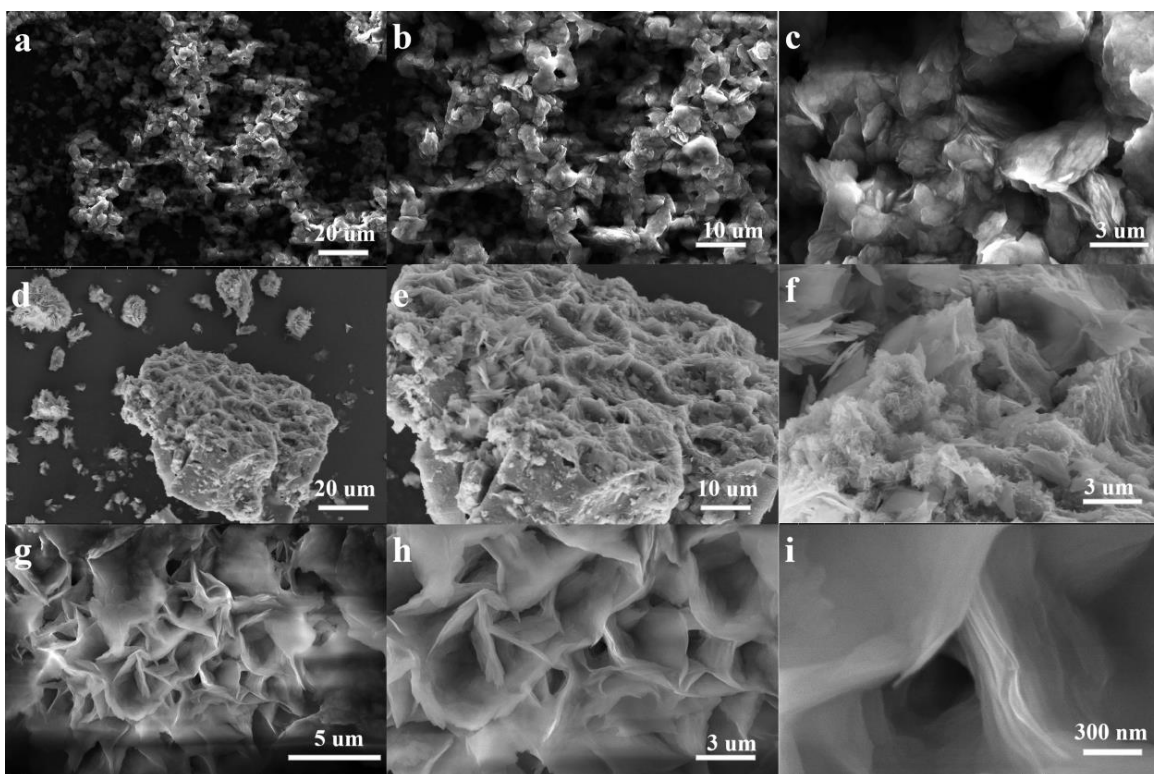


Figure 2. SEM images of Ni-MOF_{BDC}@C, (a-c): MOFs@C_P; (d-f): MOFs@C_S; (g- i): MOFs@C_{SP}

Fig. 3a and 3b show the TEM images of MOFs@C_{SP} at different magnifications. As shown in Fig. 3b, the nanosheets of MOFs@C_{SP} grow in parallel in one direction with a thickness of approximately 50 nm. The SEM and mapping of MOFs@C_{SP} are shown in Fig. 3c, and the results indicate that the elements (Ni, C and Co) in MOFs@C_{SP} are evenly distributed.

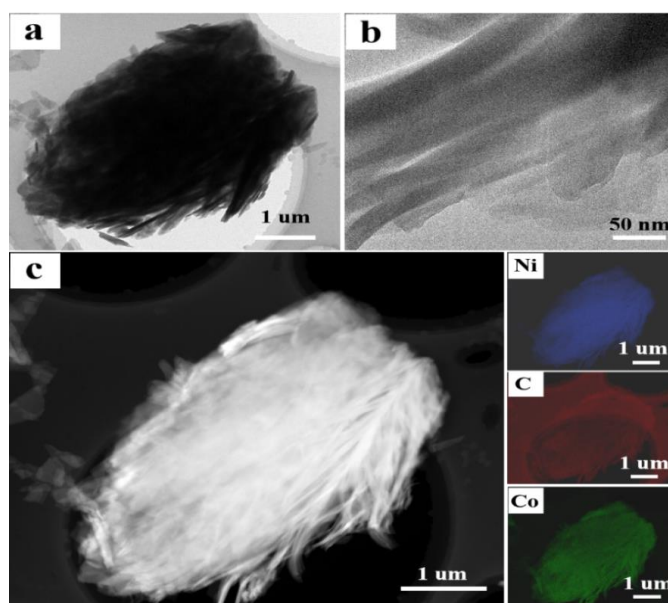


Figure 3. (a, b): TEM image of MOFs@C_{SP}; c: SEM image and mapping of MOFs@C_{SP}

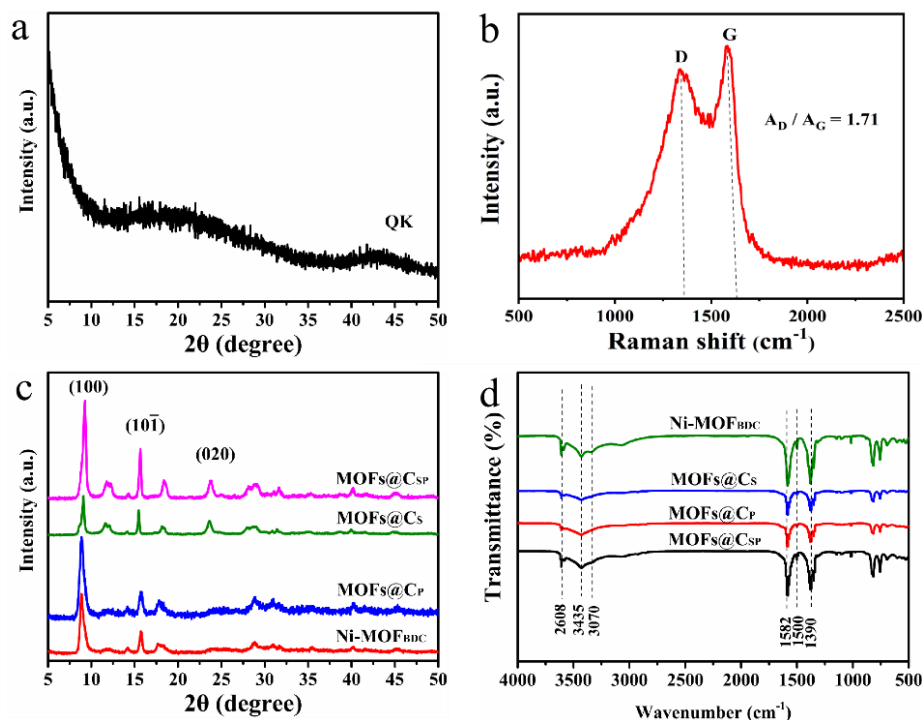


Figure 4. a: XRD pattern of QK; b: Raman spectrum of QK; c: XRD patterns of Ni-MOF_{BDC}, MOFs@C_S, MOFs@C_P and MOFs@C_{SP}; d: FTIR spectra of Ni-MOF_{BDC}, MOFs@C_S, MOFs@C_P and MOFs@C_{SP}

To obtain more detailed structural information about the samples, XRD, Raman and FT-IR tests were performed. Fig. 4a illustrates that QK is graphite carbon. Its structural characteristics and graphitization degree were characterized by Raman spectroscopy (Fig. 4b). The ratio of the D peak to the G peak is 1.7, further indicating that QK is graphitized carbon [27]. As shown in Fig. 4c, the XRD diffraction peaks for MOFs@C_S, MOFs@C_P, MOFs@C_{SP} and Ni-MOF_{BDC} are the same, indicating that MOFs@C_S, MOFs@C_P and MOFs@C_{SP} have the same crystal structure as Ni-MOF_{BDC}. Fig. 4d shows a comparison of their infrared spectra, indicating that Ni-MOF_{BDC}, MOFs@C_S, MOFs@C_P and MOFs@C_{SP} all exhibit peaks at 1582 cm⁻¹ and 1390 cm⁻¹, corresponding to the stretching pattern of the coordination carboxyl group. The peak at 1500 cm⁻¹ belongs to the vibration of the C=C bond on the benzene ring. The results further prove that MOFs@C_S, MOFs@C_P and MOFs@C_{SP} have the same crystal structure as Ni-MOF_{BDC} [28].

3.2 Electrochemistry measurements

The electrochemical performances of the samples were studied in a three-electrode cell with a 3.0 M KOH solution as the electrolyte (Fig. 5).

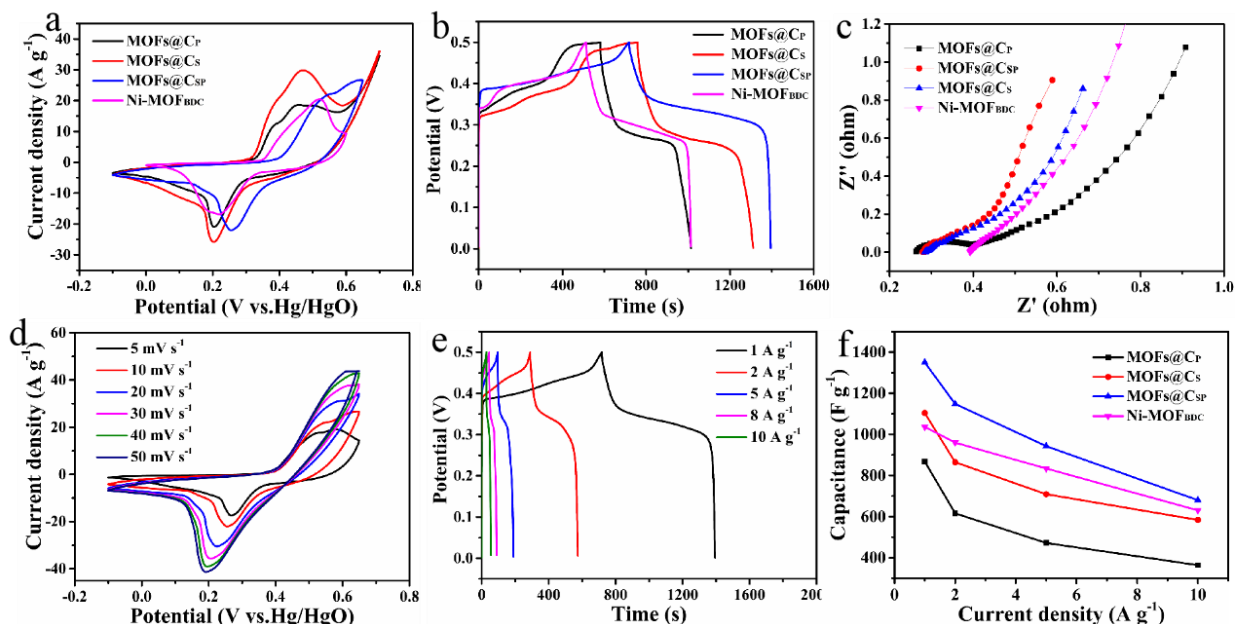


Figure 5. Electrochemical properties of MOFs@CS, MOFs@CP, MOFs@CSP and Ni-MOF_{BDC}; a: CV curves; b: GCD curves; c: EIS curves; d: CV curves of MOFs@C_{SP} at different scan rates; e: GCD curves of MOFs@C_{SP} at different current densities; f: capacitances at different current densities.

From Fig. 5a, the CV curves of MOFs@CS, MOFs@CP, MOFs@CSP and Ni-MOF_{BDC} all appear an obvious pair of redox peaks at a scanning rate of 10 mV s⁻¹, demonstrating that they all have a pseudocapacitive-type capacitance [29]. Fig. 5b shows the charge and discharge (GCD) curves of these samples at a current of 1 A g⁻¹. According to Fig. 5b, the specific capacities are 856.3 (for MOFs@CP), 1104.6 (for MOFs@CS), 1350.1 (for MOFs@CSP) and 1036.8 F g⁻¹ (for Ni-MOF_{BDC}), corresponding to coulombic efficiencies of 74.8, 71.4, 96.1 and 94.2%, respectively. This indicates that MOFs@CSP has the highest coulombic efficiency and specific capacitance among these four samples. Obviously, MOFs@CSP has the best electrochemical properties. Fig. 5c is the EIS diagram of the four samples, where the charge transfer resistances inside MOFs@CP, MOFs@CS, MOFs@CSP and Ni-MOF_{BDC} are 0.4, 0.5, 0.3 and 1.1 Ω, respectively; it proves that the addition of carbon materials can improve the conductivity of the electrode and reduce the internal charge transfer resistance [30]. The MOFs@CSP controlled by dual surfactants has the smallest charge transfer resistance because the ultrathin layer of MOFs@CSP shortens the ion migration path (Fig. 2i). More importantly, the organic combination of carbon and Ni-MOF_{BDC} under the action of dual surfactants further improves the conductivity of the material. Fig. 5d and 5e show the CV and GCD curves of MOFs@CSP. It can be seen that the CV and GCD curve of MOFs@CSP do not appear to be deformed with increasing sweep speed and current, illustrating that its structure is not destroyed by high current [31]. Fig. 5f presents the specific capacitances of MOFs@CS, MOFs@CP, MOFs@CSP and Ni-MOF_{BDC} at different current densities. As shown in Fig. 5f, the specific capacitances of MOFs@CS, MOFs@CP, MOFs@CSP and Ni-MOF_{BDC} are 623.5 F g⁻¹, 398.9 F g⁻¹, 725.6 F g⁻¹ and 680.5 F g⁻¹ under a current density of 10 A g⁻¹, respectively. It indicates that MOFs@CSP can still maintain a high specific capacitance under a high current density. This may be attributed to the relatively tight combination of Ni-MOF_{BDC} with porous

carbon in MOFs@C_{SP} and the flower-like porous structure formed by bending and folding of nanosheets grown in the same direction.

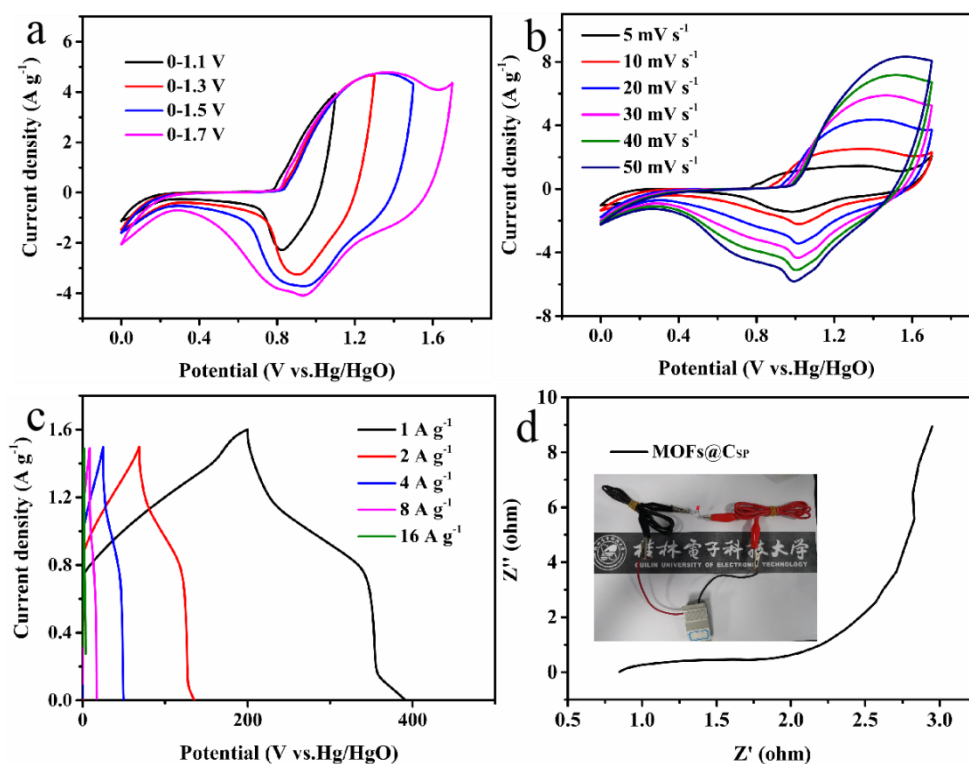


Figure 6. Electrochemical properties of MOFs@C_{SP}/NF//C/NF, a: CV curves at a scan rate of 5 mV S⁻¹; b: CV curves at different scan rates; C: GCD curves; D: EIS curve and current LED diagram.

To further study the practicability of MOFs@C_{SP} as an electrode material, an asymmetric device (MOFs@C_{SP}/nickel foam (NF)//C/NF) was assembled with MOFs@C_{SP}/NF as the positive electrode and activated carbon/NF as the negative electrode using a 3.0 M KOH aqueous solution as the electrolyte. As shown in Fig. 6a, the CV curves of the asymmetric device in different potential windows at a scan rate of 5 mV s⁻¹ demonstrate that the device has good pseudocapacitance characteristics [32]. Additionally, the CV curve is unchanged with increasing scan speed from 5 mV s⁻¹ to 50 mV s⁻¹ (Fig. 6b), indicating that the device can stably expand to the 1.7 V voltage window. Based on the GCD curve (Fig. 6c), the specific capacitances of the device at current densities of 1, 2, 4, and 8 A g⁻¹ are calculated to be 120.7, 83.2, 61.5, and 42.2 F g⁻¹, respectively. As shown in Fig. 6d, the device impedance R_{ct} is 6.3 Ω, which is better than that of Ni-MOF_{BDC} (7.5 Ω), and it can also power LED lights.

The cycle life is an important indicator to measure the performance of supercapacitors. As shown in Fig. 7, the capacity retention rate is 55.4% after 3000 cycles of MOFs@CSP/NF//C/NF at 2 A g⁻¹, and the coulombic efficiency only decreases by 5.2% after 5000 cycles. When the power density is 813.1 W kg⁻¹, the energy density of the asymmetric device reaches 42.9 Wh kg⁻¹. Compared with related references [33-37] (Table 1), it can be found that the MOFs@CSP in this work has a higher specific capacitance and power storage performance.

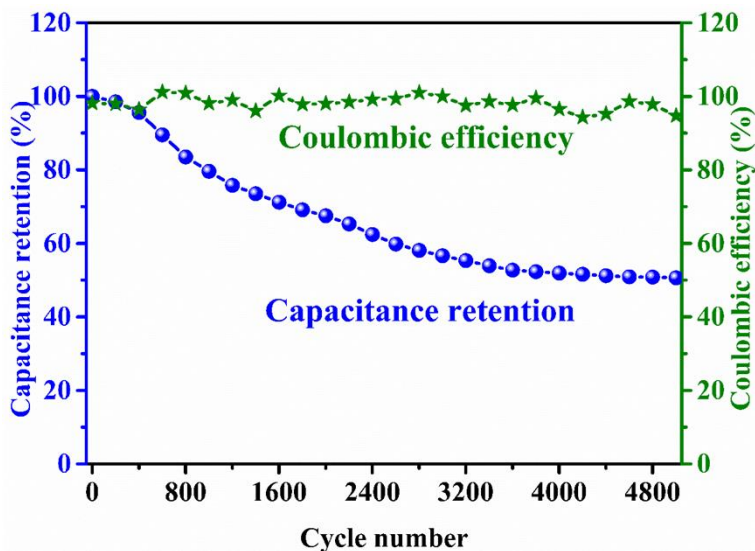


Figure 7. MOFs@C_{SP}/NF//C/NF cycle performance and Coulomb efficiency diagram

Table 1. The comparison of the capacity performances of this work with references.

Composite electrode	Electrolyte	Current density A g ⁻¹	Specific capacitance F g ⁻¹	Energy density Wh kg ⁻¹	Power density W kg ⁻¹	Reference
Co-Ni-MOF	6 M KOH	1	1300	25.92	375	[33]
Ni-MOF	2 M KOH	1	804	31.5	800	[34]
Ni-MOF	3 M KOH	1	1036	38.3	749.9	[35]
Ni-Co-S	3 M KOH	1	1377.5	36.9	1066.42	[36]
Mn/Ni-MOF	1 M KOH	1	793.6	33.2	1198	[37]
Ni-MOFs@C _{SP}	3 M KOH	1	1350.1	42.9	813.1	This work

4. CONCLUSIONS

The experimental results show that the carbon material in MOFs@C_{SP} acts as a template, which induces the growth of Ni-MOF_{BDC} along the pore orientation of the carbon to obtain a flower-like, porous structure. The specific capacity of MOFs@C_{SP} reaches 1350 F g⁻¹ at a current density of 1 A g⁻¹, which is better than that of MOFs@C_P (856.3F g⁻¹) and MOFs@C_S (1104.6F g⁻¹) prepared with the aid of a single surfactant and Ni-MOF_{BDC} (1036.8F g⁻¹) free carbon. Additionally, due to the organic combination of Ni-MOF_{BDC} with carbon under the aid of dual surfactants, the charge transfer resistance (0.3 Ω) of MOFs@C_{SP} is reduced, which is lower than that of MOFs@C_P (0.4 Ω), MOFs@C_S (0.5 Ω) and Ni-MOF_{BDC} (1.1 Ω). Furthermore, it also demonstrates that the introduction of carbon materials can enhance the conductivity of Ni-MOF_{BDC}. When MOFs@C_{SP} is assembled into an asymmetric device, the energy density reaches 42.9 Wh kg⁻¹ as the power density is 813.1 W kg⁻¹. This value is better than that of Mn/Ni-MOFs [37] (33.2 Wh kg⁻¹ at a power density of 1198 W kg⁻¹). In

conclusion, this study provides a feasible method for adjusting the morphology of MOFs to increase the pseudocapacitance of MOFs and enhance their conductivity.

ACKNOWLEDGEMENTS

This work was financially supported by the National Key Research and Development Program of China (2018YFB1502103, 2018YFB1502105), the National Natural Science Foundation of China (51971068 and 51871065), the Scientific Research and Technology Development Program of Guangxi (AA19182014, AD17195073, AA17202030-1), Guangxi Bagui Scholar Foundation, Guangxi Collaborative Innovation Centre of Structure and Property for New Energy and Materials, Guangxi Advanced Functional Materials Foundation and Application Talents Small Highlands, Chinesisch-Deutsche Kooperationsgruppe (GZ1528) and Innovation Project of GUET Graduate Education (2020YCXS112).

References

- 1 H.B. Zhang, J.W. Nai, L. Yu and X.W. Lou, *Joule*, 1 (2017) 77.
- 2 C. Zhong, Y.D. Deng, W.B. Hu, J.L. Qiao, L. Zhang and J.J. Zhang, *Chem. Soc. Rev.*, 44 (2015) 7484.
- 3 H. Wan, F.S. Chen, W. Ma, X.H. Liu and R.Z. Ma, *Nanoscale*, 12 (2020) 21479.
- 4 J.Y. Zhao and A.F. Burke, *Energy Storage Mater.*, 36 (2021) 31.
- 5 S. Sanati, R. Abazari, J. Albero, A. Morsali, H. García and L.Z. Zou, *Angew. Chem. Int. Ed.*, 60 (2021) 11048.
- 6 N.R. Chodankar, H.D. Pham, A.K. Nanjundan, J.F.S. Fernando, K. Jayaramulu, D. Golberg, Y.K. Han and D.P. Dubal, *Small*, 16 (2020) 2002806.
- 7 J.J. Zhou, W.X. Ji, L. Xu, Y. Yang, W.Q. Wang, H.L. Ding, X.C. Xu, W.W. Wang, P.L. Zhang, Z.L. Hua and L.Y. Chen, *Chem. Eng. J.*, 428 (2022) 132123.
- 8 M.R. Lukatskaya, B. Dunn and Y. Gogotsi, *Nat. Commun.*, 7 (2016) 12647.
- 9 G. Andreas and H. Llewelyn, *Nature*, 588 (2020) 28.
- 10 T.S. Mathis, N. Kurra, X.H. Wang, D. Pinto, P. Simon and Y. Gogotsi, *Adv. Energy Mater.*, 9 (2019) 1902007.
- 11 H. Liu, X. Liu, S. Wang, H. K. Liu and L. Li, *Energy Storage Mater.*, 28 (2020) 122.
- 12 J.L. Qi, Y.T. Yan, Y.F. Cai, J. Cao and J.C. Feng, *Adv. Funct. Mater.*, 31 (2021) 2006030.
- 13 L. Li, D. Zhang, J.P. Deng, Y.C. Gou, J.F. Fang, H. Cui, Y.Q. Zhao and M.H. Cao, *Carbon*, 183 (2021) 721.
- 14 D.Y. Lee, S.J. Yoon, N.K. Shrestha, S.H. Lee, H. Ahn and S.H. Han, *Microporous Mesoporous Mater.*, 153 (2012) 163.
- 15 P. Naskar, A. Maiti, P. Chakraborty, D. Kundu, B. Biswas and A. Banerjee, *J. Mater. Chem. A*, 9 (2021) 1970.
- 16 S. Zhang, Y. Zhang, F. Baig and T.F. Liu, *Cryst. Growth Des.*, 21 (2021) 3100.
- 17 Y. Kobayashi, B. Jacobs, M.D. Allendorf and J.R. Long, *Chem. Mater.*, 22 (2010) 4120.
- 18 J. Yang, C. Zheng, P.X. Xiong, Y. F. Li and M. D. Wei, *J. Mater. Chem. A*, 2 (2014), 19005.
- 19 J. Kim, C. Young, J. Lee, Y.U. Heo, M.S. Park, M.S.A. Hossain, Y. Yamauchi and J.H. Kim, *J. Mater. Chem. A*, 5 (2017) 15065.
- 20 C. Li, L. Zhang, J.Q. Chen, X.L. Li, J.W. Sun, J.W. Zhu, X. Wang and Y.S. Fu, *Nanoscale*, 13 (2021) 485.
- 21 Y.X. Chen, D. Ni, X.W. Yang, C.C. Liu, J.L. Yin and K.F. Cai, *Electrochim. Acta*, 278 (2018) 114.
- 22 Y. Yang, M.T. Hoang, A. Bhardwaj, M. Wilhelm, S. Mathur and H.X. Wang, *Nano Energy*, 94 (2022) 106910.
- 23 H.Q. Ma, B. Gao, M. Wang, Z. Y. Yuan, J. B. Shen. J. Q. Zhao and Y. K. Feng, *J. Mater. Sci.*, 56 (2021) 1064.

- 24 S. Mei, J. Zheng and W. Chu, *J. Energy Storage*, 40 (2021) 102698.
- 25 S.S. Lu, W.S. Yang, M. Zhou, L.R. Qiu, B.F. Tao, Q. Zhao, X.H. Wang, L. Zhang, Q. Xie and Y.J. Ruan, *J. Colloid Interf. Sci.*, 610 (2022) 1088.
- 26 S. Vargheese, D. Muthu, D. Pattappan, K.V. Kavya, R.T.R. Kumar and Y. Haldorai, *Electrochim. Acta*, 364 (2020) 137291.
- 27 J. Yang, W.X. Hou, R. Pan, M. Zhou, S.Z. Zhang and Y. Zhang, *J. Alloys Compd.*, 897 (2022) 163187.
- 28 J.Q. Wang, G.X. Wang, L. Cui, D.Z. Wang, S.P. Gao, S.H. Liu, S. Liu and H.F. Xu, *J. Alloys Compd.*, 903 (2022) 163917.
- 29 S.M. Huang, X.R. Shi, C.Y. Sun, X.R. Zhang, M.R. Huang, R.Q. Liu, H. Wang and S.S. Xu, *Appl. Surf. Sci.*, 572 (2022) 151344.
- 30 W.J. Liu, F.F. Zhu, B.X. Ge, L. Sun, Y. Liu and W.D. Shi, *Chem. Eng. J.*, 427 (2022) 130788.
- 31 X.Y. Chu, F.L. Meng, W. Zhang, H. Yang, X. Xu, S. Molin, P. Jasinski, X.C. Xun and W.T. Zheng, *Nanotechnology*, 33 (2022) 205403.
- 32 L.H. Lin, X.L. Yao and L. Ma, *Int. J. Electrochem. Sci.*, 15 (2020) 7763.
- 33 J. Wang, Q. Zhong, Y.H. Xiong, D.Y. Cheng, Y.Q. Zeng and Y.F. Bu, *Appl. Surf. Sci.*, 483 (2019) 1158.
- 34 S.W. Gao, Y.W. Sui, F.X. Wei, J.Q. Qi, Q.K. Meng and Y.Z. He, *J. Mater. Sci.*, 53 (2018) 6807.
- 35 Y. W, X.P. Ding, Y.M. Luo, F. Xu, L.X. Sun, J.H. Lao, X.H. Qin, D. Cai, Y. Wang, Q.Q. Yin, T. Wang, K.X. Zhang, B. Lin, H.Z. Zhang and Y.J. Zou, *Int. J. Electrochem. Sci.*, 16 (2021) 210375.
- 36 C. Chen, M.K. Wu, K. Tao, J.J. Zhou, Y.L. Li, X. Han and L. Han, *Dalton Trans.*, 47 (2018) 5639.
- 37 Y.H. Han, J.X. Zou, L.D. Wang, L. Xing, Z.W. Xue, Y.P. Jiao and Y.H. Pang, *J. Electroanal. Chem.*, 882 (2021) 114993.